

# Shape-specific fluctuations of an active colloidal interface

Arvin Gopal Subramaniam,<sup>1,2,\*</sup> Tirthankar Banerjee,<sup>3,†</sup> and Rajesh Singh<sup>1,2,‡</sup>

<sup>1</sup>*Department of Physics, Indian Institute of Technology Madras, Chennai, India*

<sup>2</sup>*Center for Soft and Biological Matter, IIT Madras, Chennai, India*

<sup>3</sup>*Department of Physics and Materials Science, University of Luxembourg, Luxembourg, Luxembourg*

Motivated by a recently synthesizable class of active interfaces formed by linked self-propelled colloids, we investigate the dynamics and fluctuations of a phoretically (chemically) interacting active interface with roto-translational coupling. We enumerate all steady-state shapes of the interface across parameter space and identify a regime where the interface acquires a finite curvature, leading to a characteristic “C-shaped” topology, along with persistent self-propulsion. In this phase, the interface height fluctuations obey Family–Vicsek scaling but with novel exponents: a dynamic exponent  $z_h \approx 0.5$ , a roughness exponent  $\alpha_h \approx 0.9$  and a super-ballistic growth exponent  $\beta_h \approx 1.7$ . In contrast, the orientational fluctuations of the colloidal monomers exhibit a negative roughness exponent, reflecting a surprising *smoothness law*, where steady-state fluctuations diminish with increasing system size. Together, these findings point towards a unique non-equilibrium universality class associated with self-propelled interfaces of non-standard shape.

## I. INTRODUCTION

Out-of-equilibrium agents with suitably chosen interactions are known to exhibit emergent collective order, most prominently in the form of a global polar order [1, 2]. Such order can arise from alignment rules [2, 3], topological interactions [4], long-ranged attraction or repulsion [5, 6], and/or other generic behavioral couplings [7]. In parallel, a distinct body of work in statistical physics has established a deep understanding of fluctuating interfaces, where the statistical properties of the interface height obey universal scaling laws [8–11]. A cornerstone result in this field is the Family–Vicsek (FV) scaling law, which relates the roughness of the interface to the system size and time through universal exponents [12, 13]. These exponents are known for certain solvable models, such as the Edwards–Wilkinson (EW) and Kardar–Parisi–Zhang (KPZ) equations [8, 9, 14], while numerical and experimental studies have revealed a wealth of deviations, suggesting novel universality classes [15–18]. Bridging these two domains, the study of *active interfaces*, i.e., interfaces driven out of equilibrium by internal activity, is a subject of recent interest [19–24], raising new questions about how activity reshapes interfacial fluctuations and scaling behavior.

In this article, we study a polar colloidal chain as a non-equilibrium interface in  $1 + 1$  dimensions. This is inspired by recent experiments that have been able to synthesize an autophoretic polar chain via chemical self-interactions [25], as opposed to other propulsion mechanisms via external actuation [26–28]. We study the dynamical steady-states of this system and show that within a specific parameter regime the chain ballistically propels with a deterministic “C-shape” [25, 29]. As opposed to conventional growing (circular) interfaces, the

non-equilibrium interface we study here displays the additional phenomena (in addition to being propelled) of curvature acquisition during its dynamics, attained via the inter-monomeric phoretic interactions, thus adding additional time scales to the conventional early time deterministic plus late time diffusive behaviour [30]. The polar nature of the interface of this topology (and hence the reason it breaks translational symmetry and propels in a given direction) enables calculations of height fluctuations of the monomers about a mean height defined across the interface.

We report that the interface-height fluctuations of this chain obey FV scaling, characterized by a set of dynamic ( $z_h \approx 0.5$ ) and roughness ( $\alpha_h \approx 0.9$ ) exponents. Correspondingly, the fluctuations preceding the steady state are captured by a super-ballistic growth exponent  $\beta_h \approx 1.7$ . The steady-state orientational fluctuations of the colloidal monomers in the C-shape phase, in contrast, decrease with the chain length, exhibiting a *negative* roughness (i.e. “smoothness”) exponent ( $\alpha_\theta \approx -0.5$ ). Moreover, we report a distinct set of scaling exponents characterizing the locally flat regime, defined by monomer-level averages restricted to flat portions of the chain and, independently, by taking the infinite-chain limit. Given that the shape of the propelling interface does not fall under conventionally studied circular or flat interfaces [31], these exponents thus constitute a unique non-equilibrium signature of an interface with a stereotypic “C-shape” topology.

The paper is structured as follows. In Sect. II, we introduce the model and enumerate the relevant length and time scales of our model. In Sec. III, we study the dynamical regimes of the model as functions of selected dimensionless numbers and obtain a phase diagram [Fig. 1]. The main results of this paper are presented in Sec. IV, where we discuss in detail the height and orientational fluctuations of this system, in addition to the effect of finite rotational noise. We finally discuss the significance of our findings and future directions in Sec. VI.

\* ph22d800@smail.iitm.ac.in

† tirthankar.banerjee@uni.lu

‡ rsingh@physics.iitm.ac.in

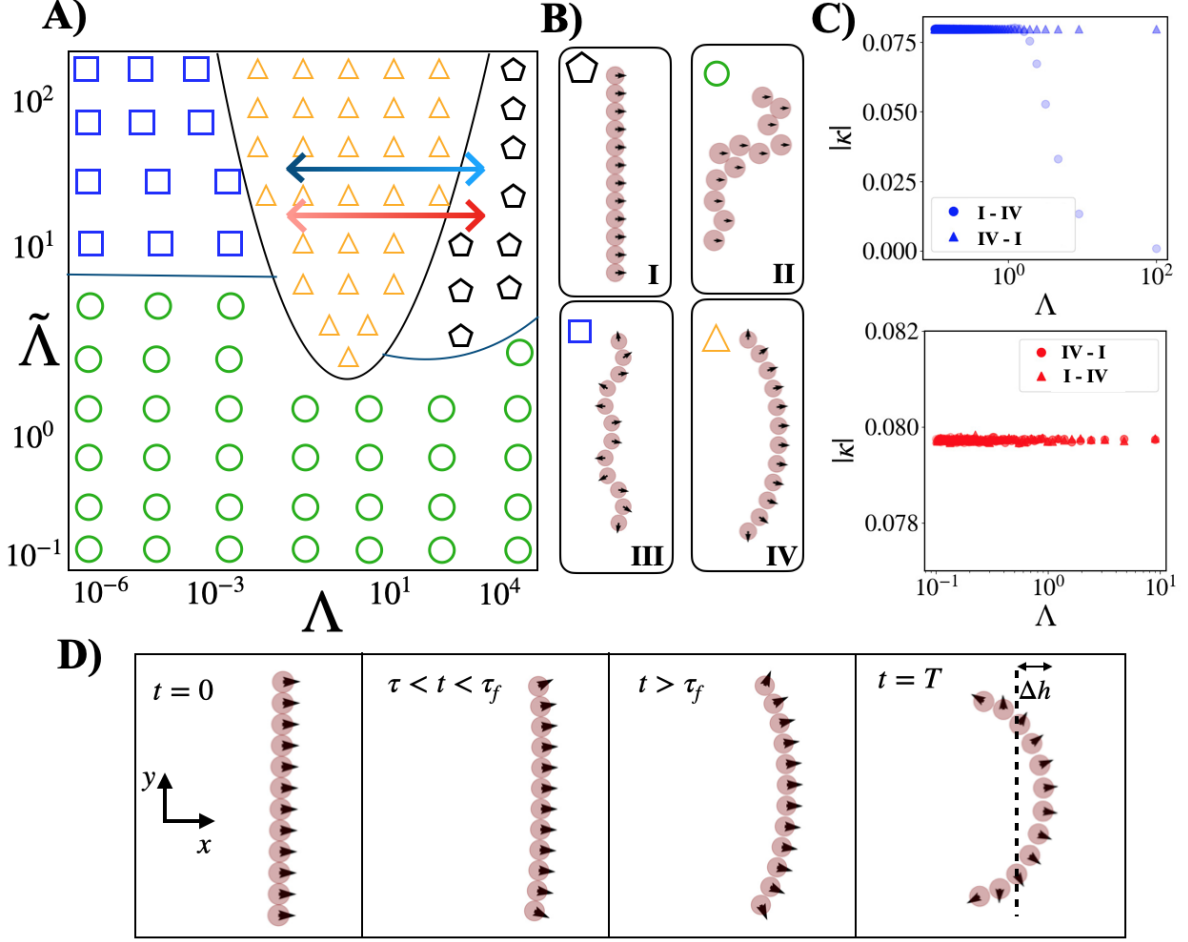


FIG. 1. **A)** Phase diagram in  $\Lambda$ - $\tilde{\Lambda}$  plane, see Eq.(7). The log absolute value of curvature has been used to delineate the phases. The phase diagram has been drawn with for a chain with  $N = 256$  number of monomers. **B)** Representative images for each phase is shown along with the marker key for a smaller chain for clarity. Values of  $(\Lambda, \tilde{\Lambda})$  are **I**:  $(10^4, 10^2)$ , **II**:  $(10^1, 10^0)$ , **III**:  $(10^{-3}, 10^2)$ , **IV**:  $(10^1, 10^2)$ . **C)** Displays the effect of selection statistics of the C-shape under two separate protocols, where the absolute value of the curvature  $|\kappa|$  has been plotted against the control parameter. *Top* corresponds to that of variation of  $\Lambda$  starting in Phase I, whilst *bottom* is starting in Phase IV. Note that  $|\kappa| \approx 0.0797$  indicates the C-shape absolute curvature. Light points denote the beginning of the protocol whilst dark the end for the forward direction, with the opposite color shading for the reverse. Color shade and parameter values correspond to arrows shown in panel **A** for transitions between states **I** and **IV** of the phase diagram. **D)** An example snapshot of the evolution in Phase IV with  $N = 12$  and  $\tau_f = 0.2$ . The rightmost snapshot shows the steady-state shape with an example mean height (vertical dotted line) and definition of  $\Delta h$  in Eq.(8).

## II. MODEL

We consider an active polymer consisting of chemically interacting active particles as monomers. The  $i$ th active particle - centered at  $\mathbf{r}_i = (x_i, y_i)$  - is confined to move in two-dimensions. It self-propels with a speed  $v_s$ , along the directions  $\mathbf{e}_i = (\cos \theta_i, \sin \theta_i)$ . The position and orientation of the  $i$ th particle are determined by the following evolution equations:

$$\dot{\mathbf{r}}_i = v_s \mathbf{e}_i + \mu \mathbf{F}_i^b + \sqrt{2D_t} \boldsymbol{\xi}_i^t, \quad (1)$$

$$\dot{\theta}_i = \chi_r (\mathbf{e}_i \times \mathbf{J}_i) + \sqrt{2D_r} \xi_i^r. \quad (2)$$

In the above equations,  $\mu$  is mobility,  $D_t$  and  $D_r$ , respectively, are translational and rotational diffusion constants of the particle, while  $\boldsymbol{\xi}^t$  and  $\boldsymbol{\xi}^r$  are white noises with zero mean and unit variances. The constant  $\chi_r$  is taken to be positive so that the particles rotate away from each other (chemo-repulsive). The force on the  $i$ th particle is given as:  $\mathbf{F}_i^b = -\partial U / \partial \mathbf{r}_i$ , while we have:  $U = \sum_{i=1}^{N-1} \mathcal{U}^b(\mathbf{r}_i, \mathbf{r}_{i+1})$ . Here,  $\mathcal{U}^b(\mathbf{r}_i, \mathbf{r}_j) = k(r_{ij} - r_0)^2$  is a harmonic potential of stiffness  $k$  and natural length  $r_0$  which holds the chain together, while  $r_{ij} = |\mathbf{r}_i - \mathbf{r}_j|$ .

The orientation of the particles, given by the angle  $\theta_i$ , changes due to coupling to a chemical (phoretic) field  $c(\mathbf{r}, t)$ . The chemical interactions between the monomers

of the chain are contained in  $\mathbf{J}_i = -\partial c / \partial \mathbf{r}_i$ , where  $c$  is the concentration of the phoretic field. It is worthwhile to note that the positional and orientational dynamics are coupled in our model. This roto-translational coupling leads to rich phenomenology of our model, as we describe below. In the steady-state, the solution of the concentration profile  $c(\mathbf{r})$  follows from the equation:  $D_c \nabla^2 c(\mathbf{r}, t) + \sum_{i=1}^N c_0 \delta(\mathbf{r} - \mathbf{r}_i) = 0$ , where  $D_c$  is the diffusion coefficient of the filled micelles and  $c_0$  is emission constant of the micelles. This gives the expression for the current:

$$\mathbf{J}_i = \frac{c_0}{4\pi D_c} \sum_{\substack{j=1 \\ j \neq i}}^N \frac{\mathbf{r}_i - \mathbf{r}_j}{|\mathbf{r}_i - \mathbf{r}_j|^3} \quad (3)$$

This current is thus interpreted as that which is instantaneously deposited on the centers of the colloids.

Variants of the above model have been studied recently [25, 29]; a detailed phase diagram of the model was obtained in [29] in terms of the dimensionless group of the system. Here, we focus on the fluctuations in the so-called ‘‘C-shape’’ phase, where the chain spontaneously acquires a stereotypic shape resembling the alphabet C, and propels in a direction normal to its tangent [25, 29]. We note that the ‘‘C-shape’’ topology we refer to is specific to systems in which roto-translational coupling in the dynamics induces the steady-state shape. The system we study being ‘‘dry’’ with such a coupling, is distinct from other similar topologies seen in (for instance) the physics of sedimenting filaments [32]. In the limit of  $N \rightarrow \infty$  it corresponds to an interface which is moving. A schematic of this is shown in Fig. 1D. We focus on the fluctuations of that moving interface in this paper.

For the entire paper (unless specified otherwise), we use the following initial conditions:

$$\theta_i(0) = 0, \quad x_i(0) = 0, \quad \forall i, \quad (4)$$

$$y_{i+1}(0) = y_i(0) + 2b, \quad 1 \leq i \leq N-1 \quad (5)$$

where  $b$  is the radius of each colloid. Note that  $r_0 = 2b$ . All numerical results in this paper are generated with an explicit Euler-Maruyama integrator with time step  $dt = 0.01$  and simulation time  $T = 7.2 \times 10^5$ . For all simulations here (unless stated otherwise)  $b = 1$ ,  $c_0 = 1$ ,  $D_c = 1$ ,  $\hat{\mu} = \mu k_b = 91.6 s^{-1}$ , and  $v_s = 1$ .  $D_r = 0$  for all sections, with the exception of Sec. VC where values are explicitly stated. Wherever realization average is performed, we use 50 realizations, with the exception of 10 used in Appendix 1.

### III. DYNAMICAL REGIMES

We first define some typical time scales, ratios of which determine the relevant dimensionless numbers needed to understand the non-equilibrium phase diagram (Fig. 1):

$$\tau = \frac{b}{v_s}, \quad \tau_t = \frac{b^2}{D_t}, \quad \tau_f = \frac{b^3}{\chi_r}, \quad \tau_r = \frac{1}{D_r}. \quad (6)$$

Here,  $\tau$  is a spontaneous propulsion time scale, which is the time it takes for an isolated particle to move a distance equaling its radius in absence of any reorientation,  $\tau_f$  sets the average time during which the orientation of the colloid changes in response to the chemical field.  $\tau_t$  and  $\tau_r$  are the time scales set by the translation noise  $D_t$  and the rotational noise  $D_r$ , respectively. Competition between these time scales gives rise to different dynamical and scaling regimes of the propelling interface.

We define two dimensionless activity parameters:

$$\Lambda = \frac{\tau_f}{\tau} = \frac{b^2 v_s}{\chi_r}, \quad \tilde{\Lambda} = \frac{\tau_t}{\tau} = \frac{b v_s}{D_t}. \quad (7)$$

The dimensionless number  $\Lambda$  quantifies the competition between deterministic rotations (due to phoretic interactions) and deterministic propulsion. The dimensionless number  $\tilde{\Lambda}$  quantifies deterministic and random motion in the positional sector. A variant on the above model, section II, was introduced in [25] and studied further in [29]. In both these papers, we had considered the role of trail created by the particles. Here, we first assume instantaneous chemical interactions, and discuss the effect of trail-mediated history later (in Appendix 1). Additionally, we note that the previous works ignored the role of translational noise  $D_t$ . In [29], it was found that a competition between  $\tau_r$  and the chemical diffusivity of trails leads to the formation of a stable C-shape chain.

It is informative to study the model described above in terms of the two dimensionless numbers. In Fig. 1, we present a phase diagram in the plane of  $\Lambda$  and  $\tilde{\Lambda}$ . We find that the C-shape is sustained for a selected range of dimensionless numbers  $\Lambda$  and  $\tilde{\Lambda}$  [25, 29]. Let us construct in addition a fluctuating length scale  $l_f = \frac{D_t}{v_s}$  and a correlation length scale  $l_C = \frac{\chi_r}{b v_s}$  to aid with the analysis. First, in the limit of  $\Lambda \gtrsim 10^2$ ,  $\tilde{\Lambda} \gtrsim 10^1$ , there exists insufficient rotations and the chain remains flat within the simulation time scale [29]. This instead corresponds to the region of extremely *short-wavelength* fluctuations ( $l_f < b$ ) and small deterministic correlation lengths ( $l_C < 10^{-3}b$ ). This straight-chain phase is labelled as Phase I (see Fig. 1(b) top left). Next, for regions  $\tilde{\Lambda} \lesssim 10^0$ , we find a disordered phase with effectively zero positional order in the chain. Here we find that  $l_f > b$ , thus we conclude that *long-wavelength* fluctuations of greater than the monomer size are not supported by our colloidal chain. This disordered phase is labelled as Phase II (Fig. 1(b) top right). Further, focusing in the regime  $\tilde{\Lambda} > 10^1$  and  $\Lambda < 10^{-3}$  corresponds to the case where deterministic rotations are instantaneous across the system ( $\tau_f \ll \tau$ ), such that the chemical interactions are instantaneously correlated. Here one has that  $l_C \gtrsim 10^3b$ , thus correlations much larger than the system size. The dynamics of the chain displays ‘‘frustrated’’ behavior, not attaining any non-trivial spatial structure as there is not enough time to respond to instantaneous

chemical gradients. This frustrated phase is labelled as Phase III (Fig. 1(c) bottom left). The remaining region corresponds to that of the C-shape (Phase IV). We thus conclude that the C-shape thus corresponds to regimes where the correlation lengths  $l_C$  are of the order of the chain length, which is in addition stable to short-wavelength fluctuations (of typical distance less than one monomer radius). It is this dynamical steady-state (DSS) phase that we study in the rest of this paper.

We also note that, within the C-shape phase, its existence as a DSS depends on the choice of initial conditions of Eq. (4). Deviating from these does not render a universality of the DSS, unless one includes the existence of chemical trails in the model [25, 29]. This scenario is further discussed in Appendix 1. If one deviates from the purely chemo-repulsive scenario considered here, the presence of trails are also necessary for other non-trivial DSS, such as the swimming/undulating state. However, various *structural* SS (e.g. designer crystallites that break handedness symmetry) is possible via the instantaneous chemical deposition model considered here, though one would have to significantly alter from the fully chemo-repulsive scenario, and incorporate mixed (anti-symmetric and/or non-reciprocal) interactions [29].

#### A. Characteristics of the C-shape

Beyond the (log) curvature of the chain, it is instructive to further distinguish the C-shape from other possible DSS that can be attained from simulation. These DSS correspond to those from the phase diagram in Fig. 1, but in addition those that are (a) in the same  $(\Lambda, \bar{\Lambda})$  coordinate but of different  $N$ , (b) adding rotational noise [29, 33], and/or (c) chemical trails in the dynamics. Fluctuations about other DSS, could in principle be legitimately computed as well. For instance in the Phase I of  $\Lambda \rightarrow \infty$  these would trivially reproduce an early-time growth for the height fluctuations, similar to that for a driven EW model, as shown explicitly in Appendix 2. We emphasize again that the fluctuations reported in this work correspond to those exclusively about the C-shape. To emphasize the uniqueness of this shape let us list some generic properties of this DSS:

1. Continuously varying orientations along the chain
2. Finite curvature along chain (or the averaged local curvature)
3. Ballistically propelling in one direction
4. Positional and orientational symmetry along the body(y) axis

As explained in Appendix 7, there are various other DSS that meet some of the above requirements but not all. For instance the aforementioned Phase I DSS satisfies

only (i), (iii) and (iv). The C-shape is unique in that it is the only DSS that meets requirements (i)-(iv), with its propulsion perpendicular to the direction of the body axis. It is in this specific phase in which the fluctuations are computed.

#### B. C-shape selection

In Phase IV, as mentioned previously, the C-shape is always attained under the initial conditions of 4. We note that in such an autophoretic chain with chemical trails this DSS is the universal solution regardless of initial conditions [25, 29] (see Appendix 1)). However, it is instructive to ask to what extent the C-shape is attained under different initial conditions.

To this end, we apply a hysteretic protocol by varying  $\Lambda$  and carrying on the final state of a given simulation to the initial conditions of the simulation at the next time step. The order parameter used to identify this DSS is the absolute value of the curvature,  $|\kappa|$ . The results of these are presented in Fig. 1(c). Two separate cases are presented, corresponding to decrease of  $\Lambda$  starting from Phase I (the stiff chain; Fig. 1(c), *top*), and increase of  $\Lambda$  starting from Phase IV (the C-shape; Fig. 1(c), *bottom*). We observe from the former that the stiff-to-C transition is irreversible. Thus, a C-shape DSS cannot lose its spatial curvature via a decrease in self-phoretic torques. From the latter we see that the C-to-stiff transition is hence not permitted; both forward and backward sweeps of the protocol do not change the overall curvature. We also note that we have separately varied  $\bar{\Lambda}$  to and from Phase IV (not shown here); the results of these indicate that selected random configurations of Phase II may indeed transition to IV, but again there is no clear reliable reversibility of transition to define a hysteresis loop. This irreversibility of the first transition implies that such a hysteresis curve and hence mapping to equilibrium classes of phase transitions is not well defined (indeed one may have to devise an alternate order parameter); we leave the exact characterization of the nature of the transition to and from the C-shape for future work.

We merely conclude this section by emphasizing that the C-shape is the attractor (global minimum) of our EOM (2) with initial conditions of (4). The subsequent results of this work are thus based on the assumption of instantaneous chemical depositions and the aforementioned initial conditions; we note that these may change upon incorporation of chemical trails. We display in Appendix 1 that identical growth exponents are obtained when chemical trails are present; where the C-shape is instead a universal attractor (independent of initial conditions) [29].



Section	Quantity	$\beta^{(1)}$	$\beta^{(2)}$	$\alpha$	$z = \alpha/\beta$	Figure	Remarks
VA	$W_h$	$0.25 \pm 0.01$	$1.73 \pm 0.01$	$0.90 \pm 0.03$	$0.52 \pm 0.02$	2	Phase IV - positional
VB	$W_\theta$	$1.00 \pm 0.01$	NA	$-0.48 \pm 0.02$	$-0.48 \pm 0.02$	3	Phase IV - orientational
VC	$W_h$	$0.25 \pm 0.02$	$1.73 \pm 0.03$	$0.81 \pm 0.04$	$0.47 \pm 0.03$	4	Finite $\tau_r$
	$W_\theta$	$1.00 \pm 0.02$	NA	$-0.48 \pm 0.02$	$-0.48 \pm 0.02$		
VD	$W_h$	$0.25 \pm 0.02$	NA	$1.00 \pm 0.01$	$4.00 \pm 0.30$	5	Locally flat - positional
Appendix 6	$W_\theta$	$1.00 \pm 0.01$	NA	$1.02 \pm 0.02$	$1.02 \pm 0.02$	8	Locally flat - orientational

TABLE I. Table of exponents defined in equations (8-14) of section IV. Note that  $z$  is defined such that  $\beta^{(2)}$  is in the denominator for the first and third rows, whereas  $\beta^{(1)}$  is in the denominator for the others (orientational and locally flat exponents). For the last two columns,  $z$  is taken to be  $z'$  implicitly. For comparison, we note that for a one-dimensional interface:  $\alpha^{\text{EW}} = 1/2$ ,  $\beta^{\text{EW}} = 1/4$ ;  $\alpha^{\text{KPZ}} = 1/2$ ,  $\beta^{\text{KPZ}} = 1/3$  [34, 35].

#### IV. INTERFACE FLUCTUATIONS

For the C-shape chain propelling in the positive  $x$ -direction, one can define a height function  $h(y)$  along the chain. An example of its temporal evolution is shown in Fig. 1(d). One can thus choose a particular length segment along the chain and compute the height fluctuations, and measure its root-mean-squared

$$W_h(t) = \sqrt{\langle(\Delta h)^2(t)\rangle} = \sqrt{\langle(h_i(t) - \langle h(t) \rangle)^2\rangle}, \quad (8)$$

for the C-shape. Here,  $\langle \rangle$  is taken over both the segment and realizations. We can do the same for the angular fluctuations, and define

$$W_\theta(t) = \sqrt{\langle(\Delta \theta)^2(t)\rangle} = \sqrt{\langle(\theta_i(t) - \langle \theta(t) \rangle)^2\rangle}. \quad (9)$$

The quantities of interest are both the dynamical ( $W_h(t)$  and  $W_\theta(t)$ ) and steady-state ( $W_h^{\text{ss}}(t)$  and  $W_\theta^{\text{ss}}(t)$ ) properties of these fluctuations. These are:

$$W_h(t) \sim t^{\beta_h}, \quad W_h^{\text{ss}} \sim N^{\alpha_h}, \quad (10)$$

$$W_\theta(t) \sim t^{\beta_\theta}, \quad W_\theta^{\text{ss}} \sim N^{\alpha_\theta}. \quad (11)$$

Here,  $(\beta_h, \beta_\theta)$  and  $(\alpha_h, \alpha_\theta)$  are sets of growth and roughness exponents, respectively. As we show below, the positional fluctuations can be expressed via the FV scaling law [12]

$$W_h \sim N^{\alpha_h} f_h(t/N^{z_h}), \quad z_h = \alpha_h/\beta_h, \quad (12)$$

where the scaling function  $f_h$  is given as:

$$f_h(t/N^{z_h}) \propto \begin{cases} t^{\beta_h} & t \ll t_h^*(N) \\ 1 & t \gg t_h^*(N) \end{cases} \quad (13)$$

For the orientational sector, we find that, though there is a growth followed by a plateau, there is a *persistent smoothing* phenomena, where there is no system-size dependent saturation time scale, but instead a system-size dependent scaling of the fluctuations at *all times*, which is instead negative (hence smoothness). This is further elaborated on below. In this case, the scaling reads:

$$W_\theta \sim N^{\alpha_\theta} f_\theta(t). \quad (14)$$

Here, we have defined:

$$f_\theta(t) \propto \begin{cases} t^{\beta_\theta} & t \ll t_\theta^* \\ 1 & t \gg t_\theta^* \end{cases} \quad (15)$$

with the important difference between the two being the  $N$  dependence of the characteristic saturation time of fluctuations  $t^*$ , as explained below. We note that given (15),  $W_\theta^{\text{ss}}$  can be equivalently be taken to be the time average over the entire simulation.

To compute the quantities  $W_h(t)$  and  $W_\theta(t)$  [Eq. (8) and (9)] respectively, we discuss two possibilities. There are two separate segments about which fluctuations are measurable. Let us label the length of this segment to be  $N'$ . The first obvious segment corresponds to  $N' = N$ , corresponding to the average over the entire C-shape. The second corresponds to that of a *locally flat* region; here  $N' \ll N$ , which is taken to be sufficiently far from the edges of the chain. Though established results exist for fluctuations about curved segments of an interface [9], these typically correspond to that of a (subset of a) *circular* interface, thus different from that of the C-shape (see Appendix 5). For the latter, it is to be noted that fluctuations of growing (circular) interfaces are typically measured in this regime [36, 37]; the scaling properties in this region are almost always equal to that of globally measured quantities - for instance in [16] for a flat surface and [36] for a curved surface. We discuss the specific instances of equivalences and/or differences for the C-shape below.

All the results presented in this paper are computed for  $N$  values of  $N \in [32, 64, 100, 128, 192, 200, 256, 312]$ , with curves for specific  $N$  displayed (and labelled) in each respective figure. Results for the incorporation of rotational noise are computed for  $N \in [64, 128, 192, 256, 312]$ . Choices for  $N'$  are stated explicitly in the respective section.

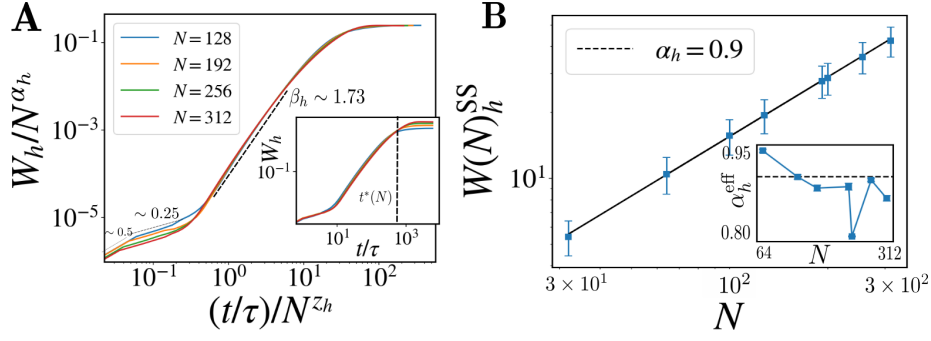


FIG. 2. Scaling of height fluctuations. **A**  $W_h$  for different chain lengths  $N$ , with the three exponents  $\beta_h$  indicated via dashed black line, fit within  $(t/\tau)N^{z_h} \in [1, 20]$ . The same scaling is plotted in the *inset*, with  $t_h^*(N)$  labelled in dashed vertical line. **B** Roughness scaling for  $W_h^{SS}(N)$ , with effective exponent in inset. Note that for the effective exponents  $N \in [64, 312]$  (excluding the smallest  $N = 32$ , due to forward-difference) Here,  $\tau_f = 0.2$ ,  $\Lambda = 0.2$ ,  $\tilde{\Lambda} = 0.01$ .

## V. RESULTS

A summary of the results in this paper is presented in Table I, wherein the respective Figures are referenced. It is to be noted that the value of  $\beta$  for each respective figure is obtained by obtaining the best collapse of the scaling relations 12 and 14 (by eye). The values for  $\alpha$  on the other hand are obtained by a least-squares fit on the steady state values of  $W$  for each system size. For each plot of  $W$ , the fitting windows used for the in-figure  $\beta$  line of best fit is mentioned in the caption.

### A. Height fluctuations

The results for the interface height fluctuations  $W_h$  are shown in Fig. 2(A). We see that there are four separate dynamical regimes, with three growth exponents which are defined as.

$$W_h(t) \sim \begin{cases} t^{\beta_h^{(0)}}, & t \ll \tau, t \ll \tau_f, \\ t^{\beta_h^{(1)}}, & \tau \ll t < \tau_f, \\ t^{\beta_h^{(2)}}, & t > \tau_f. \end{cases} \quad (16)$$

In all the three cases above  $t < t_h^*$ . Around  $t \sim t_h^*$ , the fluctuation  $W_h$  saturates to its steady-state value  $W_h^{SS}$  due to the finite system size. We now discuss these four regimes in detail.

- (i) *Early-time regime I.* This corresponds to times  $t \ll \tau$  (first few time steps of simulation). Here the growth of the interface height is dominated purely by noise, the mean-squared displacement of the height scales as  $t$ , and thus  $\beta_h^{(0)} \sim 0.5$ .
- (ii) *Early-time regime II.* Now the colloids start to feel interactions from their respective neighbors which leads to slowing down of the pure diffusive growth. Deterministic chemical self-interactions,

though, are yet to set in. Here,  $\beta_h^{(1)} \approx 0.25$ . These first two regimes correspond to those observed in the EW model [34]. For  $t < \tau_f$ , it is straightforward to show that our chain approximates an EW interface, as shown in Appendix 2. These early time scalings correspond to (as expected) a purely diffusive regime, equivalent to random deposition of particles on a substrate accompanied by surface diffusion. An alternate way to characterize the early time growth is via the probability distribution of  $W_h^2$ ; this (and a comparison with the corresponding EW distribution) is presented in Appendix 2.

- (iii) *Super-ballistic regime:* In this regime  $t > \tau_f$  with  $t < t_h^*$ . During this time, the self-phoretic interactions cause the chain to morph into a C-shape topology. As a result,  $W_h$  swells up to its steady-state value, with a super-ballistic exponent ( $\beta_h^{(2)}$ , quoted below). Let us study the behaviour of these fluctuations by defining a correlation length  $l_c$ . Via dimensional analysis,  $l_c \sim b(\frac{t}{\tau})^{\frac{1}{z_h}}$ . In this region  $l_c$  typically corresponds to a finite fraction along the interface. For instance, at  $t = 10\tau$  time steps into the simulation (at the onset of swelling, see inset of Fig. 2(A)),  $l_c \approx 53b$ . These correlations further build-up until the next regime is reached.
- (iv) *Steady-state regime.* This regime corresponds to  $t \gg \tau_f$  and  $t \gg t_h^*$ . We identify  $t_h^* = N^{z_h}\tau$ , a system-size dependent characteristic timescale over which the fluctuations reach a steady-state (see inset of Fig. 2(A)). For example for  $N = 256$  (Fig. 2(A) *inset*, green),  $t_h^* \approx 27.6\tau \sim 10^2\tau_f$ . Here, the fluctuations cease to grow and  $W_h$  reaches a plateau. The aforementioned correlations now scale as  $(\frac{t}{\tau})^{\frac{1}{z_h}} \sim N$  (spanning the entire chain length). *System size scaling.* Fig. 2(B) shows the scaling of  $W_h^{SS}$  with the chain length  $N$ ; a roughness exponent of  $\alpha_h \approx 0.9$  is found. The errorbars on coordinate points are computed by taking the standard deviation of  $W_h$  over 50 realizations in the steady-state.

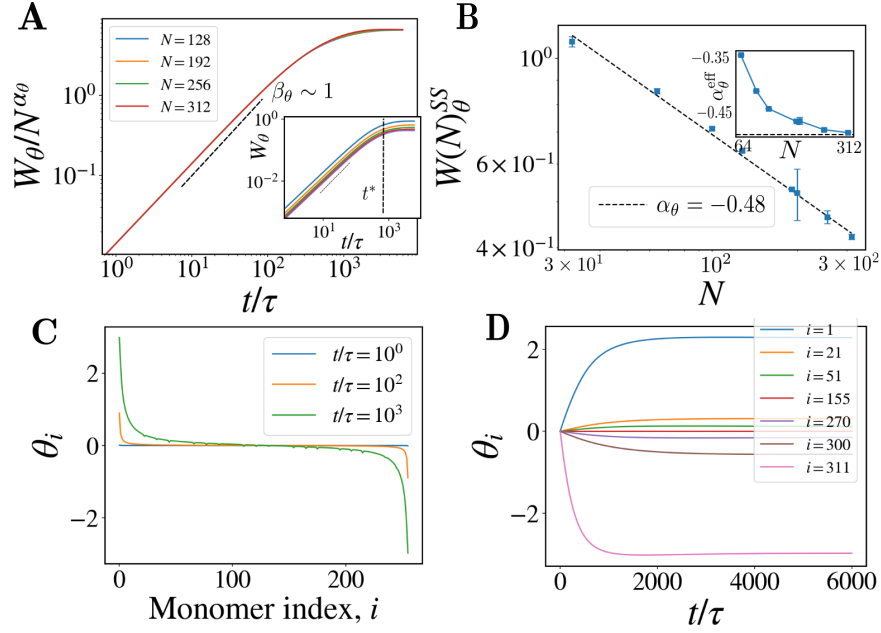


FIG. 3. Scaling of the orientation fluctuations. **A**  $W_\theta$  for different chain lengths  $N$ , with the dynamic  $\beta_\theta$  labelled (fit between  $(t/\tau N^{z_h}) \in [10, 200]$ ). The same scaling is plotted in the *inset*, with  $t^*$  labelled in dashed vertical line. **B** (Anti-) Roughness scaling for  $W_\theta^{SS}(N)$ , with effective exponent in the inset. **C** Orientation profile of the C-shape, taken at different time points. **D** Dynamical evolution of  $\theta_i$  for selected monomers  $i$ . Here,  $\tau_f = 0.2$ ,  $\Lambda = 0.2$ ,  $\tilde{\Lambda} = 0.01$ , and  $N = 311$  (for panels C and D).

In the inset the effective exponent  $\alpha_h^{\text{eff}} = \frac{d \log W_h^{SS}}{d \log N}$  is plotted. A moderate convergence is observed to the best fitted exponent of 0.9 (black dotted horizontal line in inset).

The growth and roughness exponents, respectively characterizing the height fluctuations in regimes (iii) and (iv) are:

$$\beta_h^{(2)} = 1.73 \pm 0.01 \quad (17)$$

$$\alpha_h = 0.90 \pm 0.03 \quad (18)$$

From (18) and Fig. 2, we find that regimes (iii) and (iv) exhibit a clear FV scaling with a roughness exponent  $\alpha_h$  and a dynamic exponent  $z_h = \frac{\alpha_h}{\beta_h} \approx 0.52$ . To the best of our knowledge, this set of exponents does not correspond to any previously reported universality class. We thus interpret this as a novel “C-shape roughness” scaling, distinct to those found for either circular or flat interfaces [15, 36]. The super-ballistic exponent can be appreciated by noting that as the C-shape formation takes place, displacements of each monomer from the mean is enhanced in either direction (along the x-axis) along the chain. These squared deviations from the mean height are in addition symmetric along the y-axis.  $l_c$  is clearly enhanced due to this symmetry. It is to be noted that in a conventional ballistic scaling one simply has uni-directional deviations along the propulsion axis; in our system this is applicable to the mean  $h(y)$ ; clearly  $l_c$  in this case is smaller than for a symmetric C-shape. We suggest that these combined effects give rise to

the super-ballistic growth exponent  $\beta_h$ . The presence of a super-ballistic exponent can be rationalized via a linearised analysis of the EOM 2. This is presented in Appendix 3. It is to be noted that varying  $\tau_r$  changes the time at which super-ballistic growth sets in (exponent and roughness is unchanged). The roughness exponent  $\alpha_h$ , on the other hand, indicates the relative growth of height fluctuations when  $l_c$  spans the system size. Here, the system is at  $\sim 10^2 \tau_f$  and the C-shape is fully formed. We note that the value we report is in between the standard roughness encountered in dynamics without conservation [34, 35] and smaller than models with mass conservation [17, 38, 39]. In addition larger than most numerical deposition models such as for instance the solid-on-solid growth model [16]. We discuss these discrepancies further in the Discussion section.

## B. Orientational fluctuations

The orientational fluctuations are displayed in Fig. 3(A) (and inset). There are two regimes displayed: (i) *Ballistic* regime. This corresponds to deterministic orientational changes as the C-shape forms. (ii) *Steady-state* regime.  $W_\theta$  is distinguished from  $W_h$  is that there is no  $N$  dependent  $t^*$  during which the fluctuations relax. A rough estimate of this from Fig. 3(A) would be  $t_\theta^* \sim 50 \tau_f$ , thus of the same order as  $t_h^*(N)$ . Further,  $l_c$  spans the system size at *all times* as displayed in Fig.

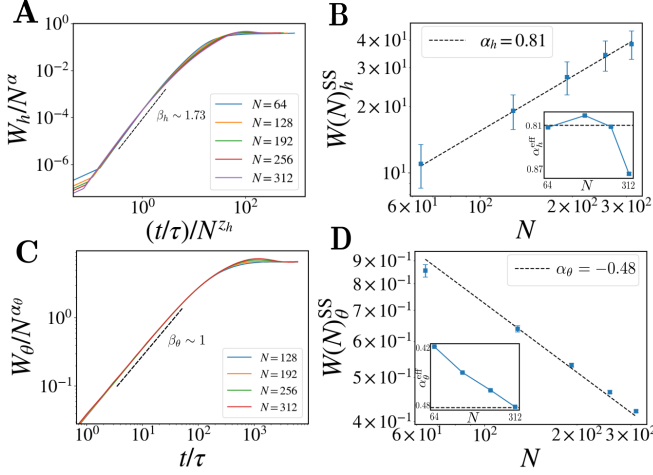


FIG. 4. Height and orientational fluctuations for finite  $\tau_r$ . **A**  $W_h$  for different chain lengths  $N$ , with the dynamic  $\beta_h$  labelled (fitting window is  $t/(\tau N^{z_h}) \in [0.5, 5]$ ). Scaling for  $W_h^{SS}(N)$ , with effective exponent in the inset. **C**  $W_\theta$  for different chain lengths  $N$ , with the dynamic  $\beta_\theta$  labelled (fitting window is  $t/(\tau N^{z_\theta}) \in [4, 80]$ ). **D** (Anti-) Roughness scaling for  $W_\theta^{SS}(N)$ , with effective exponent in the inset. Here,  $\tau_f = 0.2$ ,  $\Lambda = 0.2$ ,  $\tilde{\Lambda} = 0.01$  and  $\tau_r = 70$ .

3(A) inset.

The ballistic regime arises due to the purely deterministic contribution to the orientational changes that sets in during  $t \sim 5\tau_f \approx \tau$ . The emergence of the ballistic regime can be appreciated by consideration of the orientation profile  $\theta_i$  in Fig 3(C) for  $N = 312$ . We see that at all times  $\theta_i$  maintains strong correlations across the chain, with  $\theta_i = -\theta_{N-i}$  (anti-symmetry; here  $i$  is the monomer index). Such an anti-symmetric profile of the orientation field along the y-axis, along with the dynamics thus enforces  $l_c$  to span the entire chain length. Further, as the steady-state is approached, a large number of orientations remain close to their initial value (3(d)). For instance, if one takes a threshold  $\theta^* = 0.2$  (corresponding to  $|\frac{\max(\theta) - \theta^*}{\max(\theta)}| \approx 0.92$  deviation from the edge monomer angles), we find that a fraction of  $\approx .89$  of monomers on the chain remain roughly equal to their initial value, with the remaining  $\approx .11$  drastically varying at the edges (“orientational stiffness” [25]). We note that here  $\tau_r \rightarrow \infty$ ; the results for finite  $\tau_r$  are presented in Appendix V C; there is in addition an early time diffusive regime, though that does not affect the results presented here [40].

We further report that  $W_\theta^{SS}$  scales *negatively* with the chain length. We may thus call this a *smoothness* exponent. This form of orientational stabilization with the system size, as opposed to conventional “roughness” seen in other growing interfaces. The source of emergence for such a smoothening exponent is thus the increased ori-

entational rigidity along the chain, which increases with chain length [25]. The angular distribution along the C-shape becomes increasingly uniform, thereby making the chain stiffer and more polarized along the x-axis. The RMS deviations from the the mean orientation thus decreases with system size (a larger fraction of the chain is polarized along the x-axis). This is in contrast to the positional steady-state fluctuations, where the mean  $h(y)$  varies with chain length, and fluctuations about this exhibits roughness.

### C. With finite rotational noise

Addition of rotational noise may indeed vary the possible DSS attained from simulation. We do not report them here; but simply mention that  $\tau_r \approx 10$  sets a threshold above which the C-shape is the attractor. In this section we further investigate whether the aforementioned findings carry over to the case of finite  $\tau_r$ . Indeed we find that  $\tau_r \gtrsim 20$  an identical FV scaling for  $W_h$  is obtained, whereas  $W_\theta$  only approximates the scaling law and collapse (15) - See Fig. 4. For  $W_h$  one sees a crossover at  $\tau_r$  for the angular fluctuations between a diffusive  $\beta_\theta \approx 0.5$  and a deterministic  $\beta_\theta \approx 1$ . The effect of randomness prohibits a systems-spanning  $l_c$ . Nevertheless, a smoothness exponent with an identical scaling can be obtained.

For  $\tau_r \lesssim 10$  there is no longer a propelling C-shape, and indeed other DSS are observed. The reason for this is that the C-shape DSS is sensitive to long-wavelength fluctuations in this regime, such that any fluctuations on the length scale  $\frac{b^2 D_r}{v_s}$  is greater than typical monomer lengths. It is to be noted that for equilibrated systems  $\tau_r = \frac{8\pi\eta b^3}{k_b T}$ , with  $\tau_t = \frac{6\pi\eta b^2}{k_b T}$  ( $\eta$  the viscosity of the medium). Thus the effect of rotational noise and hence potential loss of the C-shape DSS may set in for smaller  $b$ . This trade-off and its potential experimental relevance for the system considered here is discussed further in the Discussion.

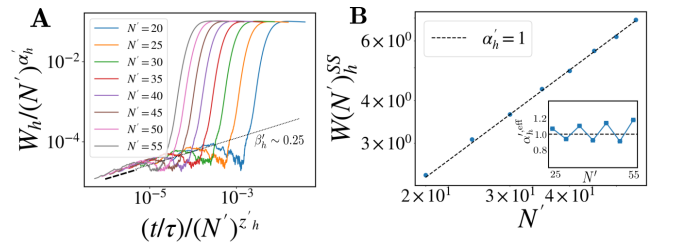


FIG. 5. Scaling of height fluctuations in locally flat region. **A**  $W_h$  for different locally flat lengths  $N'$ , with the dynamic  $\beta'_h \approx 0.25$  indicated via dashed black line, fit between  $(t/\tau N'^{z_h}) \in [5 \times 10^{-6}, 10^{-5}]$ . **B** Roughness scaling for  $W_h^{SS}(N')$ . Here,  $N = 312$  and  $\tau_f = 0.2$ ,  $\Lambda = 0.2$ ,  $\tilde{\Lambda} = 0.01$ .



### D. Locally flat regimes

In the study of fluctuations of circular interfaces, the fluctuations are typically measured about a locally flat region along the growing front [9, 36, 37]; and the roughness scalings thus correspond to those of a locally flat region. We repeat the same procedure here, and vary  $N'$  under the constraint of  $N' \ll N$ . In this section,  $\frac{N'}{N} < 0.18$  such that the interface is effectively flat. The results are presented in Fig. 5. Probing the locally flat regime, we find that the height fluctuations in the early-time ( $\beta^{(1)}$ ) and steady-state regimes, respectively, can be collapsed onto a FV-type scaling with growth exponent  $\beta'_h \approx 0.25$ , and roughness exponent  $\alpha'_h \approx 1$ . This would imply a dynamic exponent  $z'_h = 4$ . This combination of exponents is reminiscent of interfaces with conservation laws in two dimensions [17, 38, 41, 42]. However, it is to be noted that this implies essentially neglecting the super-ballistic regime, where the data does not collapse. The  $W_\theta$  scaling in this regime is presented in Appendix 6.

## VI. SUMMARY AND DISCUSSIONS

Roto-translational coupling has been well-studied for their various implications on dynamical and collective behaviour in active matter physics. The effect of this coupling on scaling laws have been established for the mean-squared displacement - i.e enhanced or anomalous diffusion - in various models (see for instance [33, 43, 44]). Here, we instead present the effect of roto-translation-induced global *topological* change, and the resultant novel scaling laws for interface fluctuations. Remarkably, we find that the height fluctuations show an FV data collapse, with a new set of dynamic and roughness exponents; with the former rationalized via a simple linearised analysis of roto-translational coupling. The orientational fluctuations, in addition, display novel scaling behaviour, notably *smoothing* with system size, which we attribute to the enhanced orientational rigidity of longer chains.

Some of our observed exponents are rationalizable via comparison with those of well-studied models. The roughness exponent 0.9 accompanying the height fluctuations is higher than that of non-conserving mass models ( $\sim 0.5$ ) and lower than conserving mass models ( $\sim 1.5$ ). These two correspond to the limit of “monomeric units” exchanging with the bulk (e.g. evaporation) and being distributed across the surface respectively. The latter limit for instance corresponds to the dynamic exponent we report in the locally flat regime (with monomeric redistribution but discounting the C-shape). We thus see why the C-shape roughness lies in between these two values - the C-shape does distribute monomeric displacements across the body (thus less suppression of large scale fluctuations), but does so whilst maintaining

a fixed bending rigidity. The growth exponent here being super-ballistic is solely a consequence of topological change due to roto-translational coupling; a simple picture as to how roto-translational coupling was give rise to super-ballistic growth is provided in Appendix 3, where an exact solution to a linearized approximate dynamics is presented (a flat chain with lowest-order roto-translational coupling). For the orientational sector, the smoothness can be appreciated by noting that as the system size increases, a proportionately larger fraction of the monomers are polarized along the x-axis, thus orientational fluctuations at larger length scales get more suppressed. The ballistic growth exponent on the other hand arises due to the deterministic effect of orientational changes that are disproportionately on the chain edges.

The emergence of novel scaling exponents [Table I], phases and transitions between them [Fig. 1] demand a thorough hydrodynamic analysis. While we defer the proposition and analysis of such a theory to future work, here we briefly outline some ingredients of a requisite continuum picture. Although individually each colloid can self-propel in any direction, the emergent macroscopic chain spontaneously breaks the isotropy by moving in a chosen direction. When the chain is in its stiff phase (I in Fig. 1), all monomers point in the same direction. However, the C-shape phase (IV in Fig. 1) arises as a result of anti-alignment of monomer orientations. At the minimal level, it may then be hypothesized that the one-dimensional chain can be modeled in terms of two dynamically coupled fields: (i) the local interface height ( $h(x, t)$ ) and (ii) the local polarization ( $\mathbf{P}(x, t) = P(\cos \theta(x, t), \sin \theta(x, t))$ ). In particular, we expect the height field to undergo noisy advection-diffusion dynamics where the advection direction is determined by the  $\mathbf{P}$  field. On the other hand,  $\mathbf{P}$  should follow a dynamics that not only allows spontaneous symmetry breaking ( $\partial_t \mathbf{P} \propto a\mathbf{P} + b|\mathbf{P}|^2\mathbf{P}$ ) but also contains alignment and anti-alignment terms ( $\partial_t \mathbf{P} \propto D_1 \nabla^2 \mathbf{P} + D_2 \nabla^4 \mathbf{P}$ ). We expect the transition from the stiff to C-shape to be accompanied by a change in sign of the coefficient of the aligning term  $D_1$ . How does  $h(x, t)$  affect the dynamics of  $\mathbf{P}$ ? For both phases I and IV of Fig. 1, the local orientation is along the local normal to the interface. In other words, the local orientation is driven by the local curvature ( $\nabla^2 h$ ) of the chain. In effect, we expect such curvature-driven polarization to then introduce non-local forces in the dynamics of the height field. Further, instead of periodic boundary conditions typically used to model growing interfaces, “clamped” boundary conditions are potentially required for the curvature to set in. These ideas provide challenges for further work.

It is of further relevance to note where these results - the existence of growth and roughness exponents that are unique to this particular topology - fit in the broader

study of active interfaces/membranes. Firstly, it is noted that non-equilibrium extensions to passive (growing) interfaces models have been theoretically proposed and new universality classes proposed. For instance, studying the capillary fluctuations on a non-equilibrium field theory, it has been shown that (in 2D)  $\alpha = 1/2$  and  $z = 3$ , whilst additional non-linear terms decreases these values slightly [23, 45, 46]. These interfaces arise from underlying scalar fields derived from conservation laws whose dynamics violate symmetries found in equilibrium. A parallel set of active membrane models are those where a Monge-like membrane is coupled to (the concentration field) a membrane-spanning protein pump that exerts a mechanical force on the membrane upon exchanging material with it (chemical coupling), with solutions to these exhibiting travelling waves [47–49]. A recent set of works study a variant of this where the protein dynamics are inclusions on the height field which hop along the membrane with an additional time scale [19, 50, 51]. For these sets of “active membrane” models, the height correlations are characterized by  $S(q) = \langle h(\mathbf{q})h(-\mathbf{q}) \rangle \sim 1/q^2$  universally, the result for a Monge (passive) interface with Gaussian fluctuations [52]. This gives rise to the standard  $\alpha = 1/2$  roughening. For orientational correlations, though these have not been studied elsewhere to our knowledge, perhaps the closest set of works pertain to those studying tangential angular correlations on a liquid–liquid interface undergoing phase separation, where the tangential angular correlations show a smoothening at large scales [21, 53]. It is evident that the physics of these aforementioned systems are starkly different from that of the autophoretic C-shape chain; we nevertheless mention them here for the sake of completion.

It remains an open challenge to verify these exponents in an experimental system. To observe significant positional fluctuations in experimental realizations, if one equates damping forces to thermal forces,  $\eta b v_s \sim k_b T/b$  ( $\eta$  the viscosity of the medium and  $v_s$  the self-propulsion  $\approx 10 \mu\text{ms}^{-1}$ ) (e.g. for droplet experiments [25, 54, 55]), one obtains  $b \approx 10^{-7}m$ , thus around 10 times smaller than typical chemically interacting colloidal systems. On the other hand, other phoretic colloidal systems (typically electrophoretic and bubble propulsion mechanisms) have reported propulsion speeds of  $v_s \sim 1 \mu\text{ms}^{-1}$  [56, 57], where the thermal fluctuations will be appreciable. Constructing extended propelling objects with a well-defined propelling interface out of these units remain an open challenge. The smaller colloids of  $b \sim 10^{-7}m$  deserve a specific consideration. These correspond to so-called “nanomotor” systems, sub-micron (mostly metallic) colloids whose synthesis routes are well established [58, 59] and have been shown to self-propel via various mechanisms [60–63]. Noting that  $\tau_r \propto b^3$ , we find that with  $b \sim 10^{-7}m$ ,  $\tau_r \sim 10^{-2}s$ , which we note is smaller than the regime required for C-shape formation to take place (c.f. Section VC). Thus, it may be feasible to

only observe the orientational growth and smoothening with an appreciable  $b \sim 10^{-6}m$ , where  $\tau_r \sim 10^1s$ , which supports the C-shape. At this scale it is also important to note that motion is no longer restricted to be in two dimensions, and continuum theories of phoretic/fluid interactions may in addition break down [64, 65]. In this context it is of interest to note recent works that have reported how phase change in 8CB liquid crystal emulsions (micron-sized) can be induced via external temperature changes [54]. In the nematic/isotropic phases, the individual colloids no longer merely deterministically self-propel but in addition have a fluctuating propulsion direction. This would correspond to finite  $\tau_r$  in our model without sacrificing monomeric size. Creating extended objects out of such systems, and/or realizing a robust C-shape with positional fluctuations thus remain an open problem. Finally, though extended colloidal chains propelled via external (as opposed to autophoretic) mechanisms have widely been synthesized [26, 27, 66–69], neither have they reported well defined shapes where interfacial height deviations and fluctuations may be readily computed - i.e. neither of these reported shapes that propel perpendicular to the body axis [29, 70]. It is noted that these systems suffer from the same translational noise suppression and noise scaling issues mentioned above.

## APPENDIX/SI

### 1. Incorporation of chemical trails

The various results quoted above have been attained via the initial conditions specified in (4) (a straight chain with parallel orientation). In this section, we further show that the height fluctuations are *universal* if one adds history-dependence (chemical trails) into the dynamics; indeed these exist in experimentally realizable chemically interacting colloidal systems [29, 71]. Thus, instead of Eq.(3), for this section, we use the following form of  $\mathbf{J}$ :

$$\mathbf{J}_i(\mathbf{r}_i, t) = \frac{c_0}{\pi b} \sum_{j=1}^N \left[ \int_0^{t-t_0} dt' \left( \frac{\Delta \mathbf{r}_{ij}}{\mathcal{D}^2} \right) \exp \left( -\frac{[\Delta \mathbf{r}_{ij}]^2}{\mathcal{D}} \right) \right],$$

$$\Delta \mathbf{r}_{ij} = \mathbf{r}_i(t) - \mathbf{r}_j(t'), \quad \mathcal{D} = D_c |t - t'|. \quad (19)$$

where  $t_0$  sets the upper bound on the memory kernel. This corresponds to monomers sensing chemical trails of their neighbors. We display the results in Fig. 6, for  $N = 250$  (note in this section  $N' = N$ ). Taking into account the timescale  $\tau_c = \frac{b^2}{D_c}$  for diffusion of filled micelles across the system, we note that it is necessary to have  $\tau_c \ll \tau_f$  with  $\tau_c \sim \tau$  to obtain the C-shape configuration [25, 29].

We present the results for  $W_h$  and  $W_\theta$  in Fig. 6 (A). We find that the scalings of  $W_h$  are reproduced. With the micellar trails, when one starts such a system

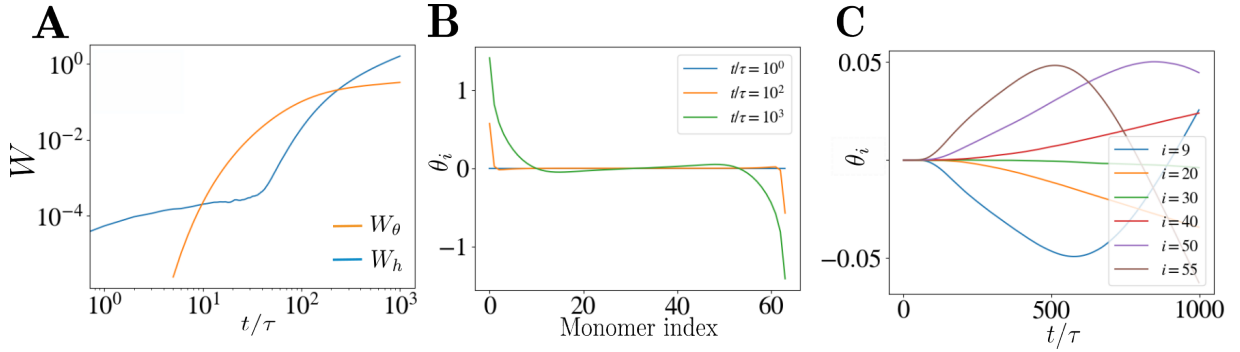


FIG. 6. Fluctuations of model with chemical trails. Example of **A**  $W_h$  and  $W_\theta$  evolution, with the dynamic  $\beta_h$  labelled (fit between  $t/(\tau N^{z_h}) \in [100, 200]$  and  $t/\tau \in [1, 10]$  respectively). **B** Orientation profile of the C-shape, taken at different time points. **C** Dynamical evolution of  $\theta_i$  for selected monomers  $i$ . Here,  $D_c = 1$ ,  $t_0 = 1$ , with  $N = 64$  and  $T = 10^5$ .

with arbitrary initial conditions (e.g. random), the trails deposited via (19) give rise to a forward-backward symmetry breaking in the orientational response to the chemicals. Thus, the system breaks the initial symmetry imposed on it and further universally picks up the C-shape. In our system, we choose sufficiently random initial conditions such that this effect is seen; we then compute  $\Delta h$  once the chain has a well-defined interface.

For this section only one system size,  $N = 64$ , was studied, averaged over 10 realizations. Note that the dynamical evolution via (19) requires at each time step a sum over all previous time steps. Thus, even for this system size (on a desktop computer with processor frequency of 2.40GHz and 16 cores), one realization takes  $3.77 \times 10^5$  seconds. Thus, a rigorous system-size determination of roughening/smoothing is prohibitive. With only one curve for  $W$ , obtaining  $\alpha$  and  $\beta$  via (12) (14) requires self-consistency. For  $W_h$ , we fix  $\alpha \approx 0.9$ ; in this setting the best fit obtained was  $\beta_h = 1.41 \pm 0.01$ . We have further checked that super-ballistic  $\beta_h$  is always obtained if the coarsening is in between evaporative and mass conserving limits (this is solely a consequence of the C-shape topology and its fixed bending rigidity, irrespective of dynamical details; see arguments in Section VI).

Further, for  $W_\theta$ , we find that fixing  $\beta_\theta = 1$  gives  $\alpha_\theta \approx 0.2$ . Thus, not a smoothing exponent, but nevertheless much less rough than the standard growth models. If one attempts to fit a negative  $\alpha_\theta$  instead, one instead finds super-ballistic orientational growth (e.g.  $\alpha_\theta \approx -0.1$  gives  $\beta_\theta \approx 4$ ). Super-ballistic growth could also be anticipated given that the time evolution contains higher order temporal derivatives, specifically for monomers near the edges (e.g.  $i = 9, 50, 55$  in Fig.6(C) versus  $i = 311$  of Fig.3(D)), thus any fluctuations about the mean will deviate from a simple ballistic scaling. On the other hand, the steady-state angular profile is no longer fully polarized along the propulsion direction (compare Fig.6(B) versus Fig.3(C)), thus  $\alpha_\theta$  is expected to be

higher than in the case without trails.

A more complete picture obviously will arise with analyses at various system sizes. However, it is safe to conclude that (i) super-ballistic positional growth; (ii) roughening of positional fluctuations; and (iii) a roughening of orientational fluctuations that is significantly less than standard models (e.g. EW/KPZ and/or Gaussian membranes) is present when chemical trails are included.

## 2. Early time approximation and probability distribution

We write down here the approximate early time dynamics for our model, showing that it represents a driven one dimensional interface and how the diffusive and subdiffusive scalings for  $W_h^2(t)$  can be accounted for. Let us explore the regime where orientation dynamics is yet to affect the translational dynamics. Let us re-write the positional dynamics of (2) for the case of the flat interface, ignoring orientation dynamics. In this case, we have

$$\frac{\partial h_i}{\partial t} = v_s + \mu \left( |h_{i+1} - h_i - 2b| - |h_i - h_{i-1} - 2b| \right) + \xi_{i,t} \quad (20)$$

Taking the continuum limit of the above, we have

$$\frac{\partial h}{\partial t} = v_s + \tilde{\mu} \frac{\partial^2 h}{\partial y^2} + \xi \quad (21)$$

which is thus a standard diffusive interface driven by a propulsion velocity  $v_s$  and a Gaussian white noise  $\xi$ . At very early times, interface fluctuations are dominated by  $\xi$ , before the diffusive term comes into play.

These height fluctuations are alternatively characterized by the distribution of fluctuations,  $P(W^2)$  [37, 72]. For the standard EW interface (non-propelling), known

results exist and are re-written here. We can directly quote the result from [72] for arbitrary initial height distribution

$$P(W^2, t) = \int_{-i\infty}^{i\infty} \frac{dy}{2\pi i} e^{xy} \prod_{n=1}^{\infty} \frac{-ys_{n0}^2 e^{-n^2\tau} / (1 + ya_n)}{\langle W^2 \rangle_{SS} (1 + ya_n)},$$

where  $W_{SS}^2 = \frac{ND_t}{12\nu_h}$ ,  $a_n = \frac{6}{(\pi n)^2} (1 - e^{-\tau_p n^2})$ , and the scaling variables are given by

$$x = \frac{W^2}{W_{SS}^2}, \quad \tau_p = \frac{8\pi^2\nu_h t}{L^2}, \quad s_{n0}^2 = \frac{2|a_n(0)|^2}{W_{SS}^2}.$$

The terms  $a_n(0)$  are Fourier transforms of the initial height profile. In our case, we start with  $h(x, t=0) = 0$ , which fixes  $a_n(0) = 0$ . For a flat initial height profile, one has  $s_{n0} = 0$ , which gives [72]:

$$P(W^2, t) = \sum_{m=1}^{\infty} \frac{1}{a_m} \frac{\exp\left[\frac{-x}{a_m}\right]}{\langle W^2 \rangle_{SS}} \prod_{n=1, n \neq m}^{\infty} \frac{a_m}{a_m - a_n}. \quad (22)$$

The early time approx of (21) corresponds to setting  $\Lambda \rightarrow \infty$ . Note that one can either  $\tau \ll \tau_f$  probe or  $\chi_r = 0$  globally; we pick the latter. The analytical distribution of (22) can then be compared to this limit; we find that the distribution is reproduced - black line and blue scatter of Fig. 7(A). We can thus suitably compare this with the case of  $\Lambda$  finite, restricting to  $\tau \ll \tau_f$ . Here, we find that our propelled interface displays deviations from this passive distribution; this is displayed in Fig. 7(B) - yellow scatter. For both cases, we plot alongside the best fit analytical distribution in dashed black, and we further find that the averaged least squared error of the fit is substantially larger in the case of  $\Lambda$  finite; we thus

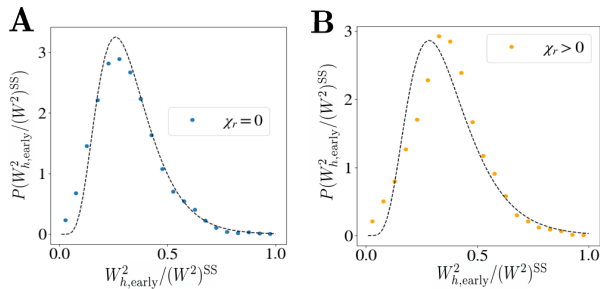


FIG. 7. **A**: Distribution of height fluctuations at early times ( $t \ll \tau_f$ ). The distribution of  $W_h^2$  of the non-interacting chain at early times (blue, scatter) can be fitted to the known exact solution for the height distribution of the EW interface; here the fitted  $\tau_p \approx 0.17$ . **B**: The chemically interacting chain (orange scatter) shows a deviation from this, with the best fit of  $\tau_p \approx 0.21$  again in dashed. The average of least squared errors for **A** and **B** are 0.0508 and 0.0728 respectively, with the latter indicating an enhanced deviation from the EW distribution. Parameters chosen are as follow: for **A**,  $\Lambda \rightarrow \infty$ , whilst for **B**,  $\Lambda = 0.2$ . In both cases  $\tilde{\Lambda} = 100$ .

conclude that the early time non-equilibrium distribution deviates from the passive EW case. This marginal deviation at early times arises again via the aforementioned roto-translational coupling; this thus again constitute a non-equilibrium signature that appears via deterministic (but small) orientational interactions. This deviation in the height distribution is analogous to that seen in so-called “anomalous diffusion” [73, 74], where microscopic colloidal particles in specific systems display a mean-squared displacement exponent of 1, but the probability distribution of displacements has been found to follow the Laplace (instead of Gaussian) distribution [74, 75]. The exact analytical distribution of the chemically interacting chain thus remains an open future problem.

### 3. Linearised approximation of super-ballistic growth exponent

In the main text we have reported the growth exponent of the C-shape to be  $\beta_h \sim 1.7$  (super-ballistic). Although rationalizing this for a curved surface is beyond exact analytical calculation in this work; we study instead a flat interface, via a the solution to the linearised approximate dynamics.

Let us study the simplest case of roto-translational coupling, in particular where (small) angular dynamics set in; in this setting the full set of equations are solvable. Consider the  $i$ th positional dynamics from (2). For small  $\theta_i$ , we can write this as

$$\dot{x}_i = v_s \left( 1 - \frac{\theta_i^2}{2} \right) + \mu F_{x_i}^b + \xi_{t,i} \quad (23)$$

Note that the  $x_i$  are assumed to be stationary in this regime (flat interface). We can use this for the angular dynamics to write

$$\dot{\theta}_i = \chi_r \left( 1 - \frac{\theta_i^2}{2} \right) S_i + \xi_{r,i} \quad (24)$$

where  $S_i = \frac{1}{4b^3} \sum_j \frac{1}{(i-j)^2} [2\Theta(i-j) - 1]$  for a completely flat chain. Here,  $\Theta(x)$  is the step function. This simplification allows us to write a linearized (24), without accounting for chemical currents along the  $x$  direction. We note that fluctuations along the body axis ( $y$  direction) mean that  $S_i$  is random quantity at each time step. The deterministic solution to this is

$$\theta_i = \sqrt{2} \frac{1 - \exp[-\chi_r S_i t]}{\exp[-\chi_r S_i t] + 1} \quad (25)$$

We next probe the early time regime of  $t \ll \tau_f$ ; this corresponds to the approximation of a flat surface (c.f. Fig. 1(d)). We then plug (25) into (23). We then use the small argument expansion for  $\cosh(z) \approx 1 + \frac{z^2}{2}$ , with



$z = \frac{\chi_r S_i t}{2}$ . This gives us

$$\dot{x}_i = F_i(t) \approx v_s \left( 1 - \frac{b^6}{2\tau_f^2} S_i^2 t^2 \right) + F_{x,i}^b + \xi_{t,i} \quad (26)$$

thus

$$\langle X \rangle = v_s t - \frac{b^6}{6\tau_f^2} \langle S^2 \rangle t^3 \quad (27)$$

where  $\langle \rangle$  is performed over both the monomers and realizations. For a flat chain (no displacements along propulsion direction),  $S_i$  is given by the deterministic formula above. In general, Here,  $X$  is a site-independent average of the chain position. We obtain the scaling for  $(\Delta h)^2$  as follows

$$W_h^2 \approx \frac{b^6}{6\tau_f^2} \langle (S_i^2 - \langle S \rangle^2)^2 \rangle t^6 + 2D_t t \quad (28)$$

where we have used that  $\langle F^b(t') \rangle = 0$  and  $\langle F^b(t') F^b(t') \rangle = \langle F^b(t) \rangle \langle F^b(t') \rangle$ . Strictly speaking, the latter will cease to be true when curvature sets in (spring forces then become correlated), but it will suffice for the flat approximation used here. We thus obtain the result that the dynamics is super-ballistic with exponent  $\sim 3$  (with an early time diffusive  $\sim 0.5$ ). Here, fluctuations along the body axis minimally accounted for such that  $\text{Var}(S) \neq 0$ . We thus conclude that minimal roto-translational coupling on a flat interface can predict diffusive to super-ballistic growth transitions but clearly overestimates the super-ballistic exponent to that of a surface with finite curvature.

#### 4. Early-time approximation to ballistic orientational growth

The deterministic solution on a quasi-flat chain also enables us to rationalize the  $\beta_\theta \sim 1$  at early times. From (25), let us probe  $t \ll \tau_f$ , where we find

$$\theta_i \approx \frac{1}{\sqrt{2}} (\chi_r S_i t) \left[ 1 + \frac{\chi_r S_i t}{2} \right] \quad (29)$$

Next, we exploit the symmetries of the orientations along the body axis (c.f. Fig. 3(c)), where we find that  $\langle \theta \rangle_i = 0$  and by extension  $\langle (\Delta \theta)^2 \rangle = \langle (\theta_i - \langle \theta \rangle_i)^2 \rangle = \langle \theta_i^2 \rangle$ . Thus

$$\langle (\Delta \theta)^2 \rangle = \langle \theta_i^2 \rangle = \frac{b^6}{2\tau_f^2} \langle S_i^2 \rangle t^2 + O(t^3) + O(t^4) \quad (30)$$

where the terms  $O(t^{3,4})$  are sub-leading for  $t \ll \tau_f$ . Thus, a combination of the symmetry of the orientations along the chain ( $\theta_i = -\theta_{N-i}$ ) and the transverse fluctuations approximation of the previous section gives us  $\beta_\theta \sim 1$  at early times.

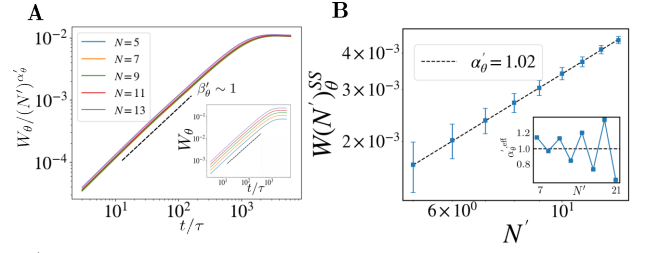


FIG. 8. Scaling of orientational fluctuations in locally flat region. **A**  $W_\theta$  for different locally flat lengths  $N'$ , with the dynamic  $\beta'_\theta$  labelled (fitting window identical to Fig. 3). The same scaling is plotted in the *inset*. **B** Roughness scaling for  $W_\theta^{\text{SS}}(N')$ . Here,  $N = 312$  and  $\tau_f = 0.2$ ,  $\Lambda = 0.2$ ,  $\tilde{\Lambda} = 0.01$ .

#### 5. Curvature of chain

To calculate the phase diagram in Fig. 1, we use the Monge representation to calculate the curvature in the steady-state [52], following [29]. We compute the curvature as:

$$\kappa = \left\langle \nabla \cdot \left[ \nabla h_i / \sqrt{1 + |\nabla h_i|^2} \right] \right\rangle, \quad (31)$$

where  $h_i$  is the height function of the chain, evaluated at each monomer location, measured from the vertical line connecting the edge monomers. The average is performed across the monomers in the chain, giving a scalar value. In our case, the inner bracket is simply reduced to  $\partial_y [\partial_y x_i(y) / \sqrt{1 + |\partial_y x_i|^2}]$ . For Fig. 1, we take the averaged  $|\kappa|$  in the steady state. Further, we note that  $\kappa \rightarrow 0$  as  $N \rightarrow \infty$  [29]. For a circular interface,  $\kappa$  would be scale as  $1/R$  ( $R$  the radius of the circle), whereas for a flat interface  $\kappa$  would be constant. Thus, this variation the  $\kappa$  profile can be used as proxy definition for the C-shape.

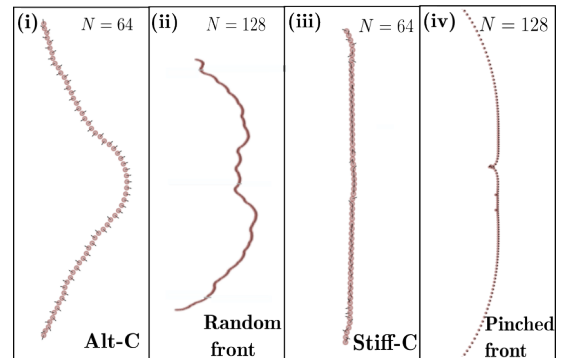


FIG. 9. Examples of DSS. From left to right: (i) Alt-C, (ii) Random front, (iii) Stiff-C, and (iv) Pinched front respectively.  $\{\Lambda, \tilde{\Lambda}\}$  values are (i)  $\{10^{-5}, 2\}$ , (ii)  $\{0.05, 0.2\}$ , (iii)  $\{10^{-6}, 200\}$ , (iv)  $\{10^1, 200\}$ . Note that (iv) in addition incorporated trails via (19); here  $t_0 = 1$  and  $\tau_r = 5$  in addition.



## 6. Scaling of $W_\theta$ in the locally flat regime

The scalings of  $W_\theta$  in for  $N' \ll N$  is presented in Fig. 8. We find that the scaling law of Eq. (14) is satisfied; the ballistic  $\beta'_\theta = 1$  is retained whilst the roughness  $\alpha'_\theta \approx 1.02 \pm 02$  is obtained. Note that this is opposed to the smoothness exponent obtained on the full C-shape. We also note that the specific choice of  $N' \in [5, 21]$  used here, thus at most  $\approx 4\%$  of the chain length, is substantially smaller than in Fig. 5. For any appreciably larger  $N'$  the scaling of (14) is not observed. These results thus further highlight the fact that the smoothness exponent found in Fig. 3 is a sole consequence of the C-shape; with distinct topology specific results vis-a-viz a flat surface.

## 7. Other DSS for large $N$

It is to be noted also that the phase diagram in Fig. 1 being  $N$  specific and only comparing  $(\Lambda, \tilde{\Lambda})$  does exclude other DSS that arise from simulation. Examples of these are shown in Fig. 9. Four examples are shown, we label them as (i) “Alt-C”, (ii) “Random front”, (iii) “Stiff-C”, and (iv) “Pinched front” respectively. We

note that DSS(ii) corresponds to the “Disordered” phase in Fig. 1. For each of these DSS, the chain propels in a deterministic direction along the x-axis; thus (8) can be computed in principle. However, none of these DSS satisfy all the criteria enumerated in Sec. III A. For DSS(i)-(iv), criteria (i) 2, 3, and 4, (ii) 1 and 3, (iii) 1, 3 and 4; and (iv) 2 and 3 are satisfied. Thus, the C-shape is the unique topology that satisfies all four criteria. The hypothetical fluctuations for  $W_\theta$  for these can also in principle be computed, but we do not pursue it here.

## ACKNOWLEDGMENTS

We thank Professors ME Cates and M Muthukumar for useful discussions. We also thank an anonymous referee for their feedback and suggestions, which led to an improvement in the presentation of our results. AGS acknowledges funding from the DIA Fellowship from the Government of India. TB is supported through the Luxembourg National Research Fund (FNR), grant reference C22/MS/17186249.

- 
- [1] J. Toner, *The Physics of Flocking: Birth, Death, and Flight in Active Matter* (Cambridge University Press, 2024).
  - [2] T. Vicsek, A. Czirók, E. Ben-Jacob, I. Cohen, and O. Shochet, Novel type of phase transition in a system of self-driven particles, *Physical review letters* **75**, 1226 (1995).
  - [3] H. Chaté, F. Ginelli, G. Grégoire, and F. Raynaud, Collective motion of self-propelled particles interacting without cohesion, *Physical Review E—Statistical, Nonlinear, and Soft Matter Physics* **77**, 046113 (2008).
  - [4] M. Ballerini, N. Cabibbo, R. Candelier, A. Cavagna, E. Cisbani, I. Giardina, V. Lecomte, A. Orlandi, G. Parisi, A. Procaccini, *et al.*, Interaction ruling animal collective behavior depends on topological rather than metric distance: Evidence from a field study, *Proceedings of the national academy of sciences* **105**, 1232 (2008).
  - [5] L. Caprini and H. Löwen, Flocking without alignment interactions in attractive active brownian particles, *Physical Review Letters* **130**, 148202 (2023).
  - [6] A. G. Subramaniam, S. Adhikary, and R. Singh, Minimal mechanism for flocking in phoretically interacting active colloids, *arXiv preprint arXiv:2504.07050* (2025).
  - [7] R. Grossmann, L. Schimansky-Geier, and P. Romanczuk, Self-propelled particles with selective attraction–repulsion interaction: from microscopic dynamics to coarse-grained theories, *New Journal of Physics* **15**, 085014 (2013).
  - [8] M. Kardar, Nonequilibrium dynamics of interfaces and lines, *Physics reports* **301**, 85 (1998).
  - [9] A.-L. Barabási and H. E. Stanley, *Fractal concepts in surface growth* (Cambridge university press, 1995).
  - [10] P. L. Krapivsky, S. Redner, and E. Ben-Naim, *A kinetic view of statistical physics* (Cambridge University Press, 2010).
  - [11] D. S. Dean, S. N. Majumdar, and S. Sabhapandit, Exact height distribution in one-dimensional Edwards–Wilkinson interface with diffusing diffusivity, *Journal of Physics A: Mathematical and Theoretical* **58**, 235002 (2025).
  - [12] T. Vicsek and F. Family, Dynamic scaling for aggregation of clusters, *Physical Review Letters* **52**, 1669 (1984).
  - [13] K. Fujimoto, R. Hamazaki, and Y. Kawaguchi, Family-vicsek scaling of roughness growth in a strongly interacting bose gas, *Physical Review Letters* **124**, 210604 (2020).
  - [14] I. Corwin, The kardar–parisi–zhang equation and universality class, *Random matrices: Theory and applications* **1**, 1130001 (2012).
  - [15] F. Family and T. Vicsek, Scaling of the active zone in the eden process on percolation networks and the ballistic deposition model, *Journal of Physics A: Mathematical and General* **18**, L75 (1985).
  - [16] J. Kim, J. Kosterlitz, and T. Ala-Nissila, Surface growth and crossover behaviour in a restricted solid-on-solid model, *Journal of Physics A: Mathematical and General* **24**, 5569 (1991).
  - [17] S. D. Sarma and P. Tamborenea, A new universality class for kinetic growth: One-dimensional molecular-beam epitaxy, *Physical review letters* **66**, 325 (1991).
  - [18] M. Degawa, T. Stasevich, W. Cullen, A. Pimpinelli, T. L. Einstein, and E. D. Williams, Distinctive fluctuations in a confined geometry, *Physical review letters* **97**, 080601 (2006).

- [19] F. Cagnetta, M. Evans, and D. Marenduzzo, Active growth and pattern formation in membrane-protein systems, *Physical Review Letters* **120**, 258001 (2018).
- [20] Q. Goutaland, F. van Wijland, J.-B. Fournier, and H. Noguchi, Binding of thermalized and active membrane curvature-inducing proteins, *Soft Matter* **17**, 5560 (2021).
- [21] R. Adkins, I. Kolvin, Z. You, S. Witthaus, M. C. Marchetti, and Z. Dogic, Dynamics of active liquid interfaces, *Science* **377**, 768 (2022).
- [22] F. Caballero, A. Maitra, and C. Nardini, Interface dynamics of wet active systems, *Phys. Rev. Lett.* **134**, 087105 (2025).
- [23] M. E. Cates and C. Nardini, Active phase separation: new phenomenology from non-equilibrium physics, *Reports on Progress in Physics* **88**, 056601 (2025).
- [24] R. Maire, A. Plati, F. Smalenburg, and G. Foffi, Conservation laws and slow dynamics determine the universality class of interfaces in active matter, *arXiv preprint arXiv:2511.18947* (2025).
- [25] M. Kumar, A. Murali, A. G. Subramaniam, R. Singh, and S. Thutupalli, Emergent dynamics due to chemohydrodynamic self-interactions in active polymers, *Nature Commun.* **15**, 4903 (2024).
- [26] D. Nishiguchi, J. Iwasawa, H.-R. Jiang, and M. Sano, Flagellar dynamics of chains of active janus particles fueled by an AC electric field, *New J. Phys.* **20**, 015002 (2018).
- [27] A. Snezhko and I. S. Aranson, Magnetic manipulation of self-assembled colloidal asters, *Nat. Mater.* **10**, 698 (2011).
- [28] B. Biswas, R. K. Manna, A. Laskar, P. S. Kumar, R. Adhikari, and G. Kumaraswamy, Linking catalyst-coated isotropic colloids into “active” flexible chains enhances their diffusivity, *ACS Nano* **11**, 10025 (2017).
- [29] A. G. Subramaniam, M. Kumar, S. Thutupalli, and R. Singh, Rigid flocks, undulatory gaits, and chiral foldamers in a chemically active polymer, *New Journal of Physics* **26**, 083009 (2024).
- [30] X.-L. Wu and A. Libchaber, Particle diffusion in a quasi-two-dimensional bacterial bath, *Phys. Rev. Lett.* **84**, 3017 (2000).
- [31] K. A. Takeuchi, An appetizer to modern developments on the kardar–parisi–zhang universality class, *Physica A: Statistical Mechanics and its Applications* **504**, 77 (2018).
- [32] L. Li, H. Manikantan, D. Saintillan, and S. E. Spagnolie, The sedimentation of flexible filaments, *Journal of Fluid Mechanics* **735**, 705 (2013).
- [33] R. Golestanian, Anomalous diffusion of symmetric and asymmetric active colloids, *Physical review letters* **102**, 188305 (2009).
- [34] S. F. Edwards and D. Wilkinson, The surface statistics of a granular aggregate, *Proceedings of the Royal Society of London. A. Mathematical and Physical Sciences* **381**, 17 (1982).
- [35] M. Kardar, G. Parisi, and Y.-C. Zhang, Dynamic scaling of growing interfaces, *Physical Review Letters* **56**, 889 (1986).
- [36] K. A. Takeuchi and M. Sano, Universal fluctuations of growing interfaces: evidence in turbulent liquid crystals, *Physical review letters* **104**, 230601 (2010).
- [37] K. A. Takeuchi and M. Sano, Evidence for geometry-dependent universal fluctuations of the kardar–parisi–zhang interfaces in liquid-crystal turbulence, *Journal of Statistical Physics* **147**, 853 (2012).
- [38] W. W. Mullins, Theory of thermal grooving, *Journal of Applied Physics* **28**, 333 (1957).
- [39] D. Wolf and J. Villain, Growth with surface diffusion, *Europhysics Letters* **13**, 389 (1990).
- [40] As explained in [29], sufficiently large rotational noise prohibits the C-shape formation. Thus, “positive  $D_r$ ” wherever mentioned here implicitly assumes  $\frac{\tau_f}{\tau_r} = \frac{b^3 D_r}{\chi_r} \ll 1$ . Here,  $\frac{\tau_f}{\tau_r} = 0.01$ .
- [41] T. Sun, H. Guo, and M. Grant, Dynamics of driven interfaces with a conservation law, *Phys. Rev. A* **40**, 6763 (1989).
- [42] T. Banerjee and A. Basu, Symmetries and scaling in generalised coupled conserved kardar–parisi–zhang equations, *Journal of Statistical Mechanics: Theory and Experiment* **2018**, 013202 (2018).
- [43] C. Bechinger, R. Di Leonardo, H. Löwen, C. Reichhardt, G. Volpe, and G. Volpe, Active particles in complex and crowded environments, *Rev. Mod. Phys.* **88**, 045006 (2016).
- [44] C. Kurzthaler and T. Franosch, Intermediate scattering function of an anisotropic brownian circle swimmer, *Soft Matter* **13**, 6396 (2017).
- [45] G. Fausti, E. Tjhung, M. E. Cates, and C. Nardini, Capillary interfacial tension in active phase separation, *Physical review letters* **127**, 068001 (2021).
- [46] M. Besse, G. Fausti, M. E. Cates, B. Delamotte, and C. Nardini, Interface roughening in nonequilibrium phase-separated systems, *Physical Review Letters* **130**, 187102 (2023).
- [47] S. Ramaswamy, J. Toner, and J. Prost, Nonequilibrium fluctuations, traveling waves, and instabilities in active membranes, *Physical review letters* **84**, 3494 (2000).
- [48] S. Ramaswamy and M. Rao, The physics of active membranes, *Comptes Rendus de l’Académie des Sciences-Series IV-Physics-Astrophysics* **2**, 817 (2001).
- [49] J.-B. Manneville, P. Bassereau, S. Ramaswamy, and J. Prost, Active membrane fluctuations studied by micropipet aspiration, *Physical Review E* **64**, 021908 (2001).
- [50] F. Cagnetta, M. R. Evans, and D. Marenduzzo, Statistical mechanics of a single active slider on a fluctuating interface, *Physical Review E* **99**, 042124 (2019).
- [51] F. Cagnetta, M. R. Evans, and D. Marenduzzo, Kinetic roughening in active interfaces, in *EPJ Web of Conferences*, Vol. 230 (EPJ Web of Conferences, 2020) p. 00001.
- [52] W. Helfrich, Elastic properties of lipid bilayers: theory and possible experiments, *Z. Naturforsch* **28**, 693 (1973).
- [53] L. Zhao, P. Gulati, F. Caballero, I. Kolvin, R. Adkins, M. C. Marchetti, and Z. Dogic, Asymmetric fluctuations and self-folding of active interfaces, *Proceedings of the National Academy of Sciences* **121**, e2410345121 (2024).
- [54] M. Kumar, S. Sane, A. Murali, and S. Thutupalli, Temperature switchable self-propulsion activity of liquid crystalline microdroplets, *Soft Matter* **21**, 3782 (2025).
- [55] S. Thutupalli, D. Geyer, R. Singh, R. Adhikari, and H. A. Stone, Flow-induced phase separation of active particles is controlled by boundary conditions, *Proc. Natl. Acad. Sci.* **115**, 5403 (2018).
- [56] J. R. Howse, R. A. L. Jones, A. J. Ryan, T. Gough, R. Vafabakhsh, and R. Golestanian, Self-motile colloidal particles: From directed propulsion to random walk, *Phys. Rev. Lett.* **99**, 048102 (2007).

- [57] S. J. Ebbens and J. R. Howse, In pursuit of propulsion at the nanoscale, *Soft Matter* **6**, 726 (2010).
- [58] J. Zhang, B. A. Grzybowski, and S. Granick, Janus particle synthesis, assembly, and application, *Langmuir* **33**, 6964 (2017).
- [59] F. Novotný, H. Wang, and M. Pumera, Nanorobots: machines squeezed between molecular motors and micromotors, *Chem* **6**, 867 (2020).
- [60] T. Lee, M. Alarcoón-Correa, C. Miksch, K. Hahn, J. G. Gibbs, and P. Fischer, Self-propelling nanomotors in the presence of strong brownian forces, *Nano letters* **14**, 2407 (2014).
- [61] S. Sánchez, L. Soler, and J. Katuri, Chemically powered micro-and nanomotors, *Angewandte Chemie International Edition* **54**, 1414 (2015).
- [62] H. Zhou, C. C. Mayorga-Martinez, S. Pané, L. Zhang, and M. Pumera, Magnetically driven micro and nanorobots, *Chemical Reviews* **121**, 4999 (2021).
- [63] S. Song, H. Han, J. Wang, Y. Pu, J. Shao, J. Xie, H. Che, J. C. van Hest, and S. Cao, Polymersome-based nanomotors: preparation, motion control, and biomedical applications, *Chemical Science* **16**, 7106 (2025).
- [64] I. Santiago, Nanoscale active matter matters: Challenges and opportunities for self-propelled nanomotors, *Nano Today* **19**, 11 (2018).
- [65] X. Ju, C. Chen, C. M. Oral, S. Sevim, R. Golestanian, M. Sun, N. Bouzari, X. Lin, M. Urso, J. S. Nam, *et al.*, Technology roadmap of micro/nanorobots, *ACS nano* (2025).
- [66] G. Jayaraman, S. Ramachandran, S. Ghose, A. Laskar, M. S. Bhamla, P. S. Kumar, and R. Adhikari, Autonomous motility of active filaments due to spontaneous flow-symmetry breaking, *Physical Review Letters* **109**, 158302 (2012).
- [67] A. Aubret, M. Youssef, S. Sacanna, and J. Palacci, Targeted assembly and synchronization of self-spinning microgears, *Nature Physics* **14**, 1114 (2018).
- [68] K. Prathyusha, F. Ziebert, and R. Golestanian, Emergent conformational properties of end-tailored transversely propelling polymers, *Soft Matter* **18**, 2928 (2022).
- [69] J. Zhang and S. Granick, Natural selection in the colloid world: active chiral spirals, *Farad. Disc.* **191**, 35 (2016).
- [70] A. Kumar, A. Maitra, M. Sumit, S. Ramaswamy, and G. Shivashankar, Actomyosin contractility rotates the cell nucleus, *Sci. Rep.* **4**, 3781 (2014).
- [71] C. Jin, C. Krüger, and C. C. Maass, Chemotaxis and autochemotaxis of self-propelling droplet swimmers, *Proceedings of the National Academy of Sciences* **114**, 5089 (2017).
- [72] T. Antal and Z. Rácz, Dynamic scaling of the width distribution in Edwards-Wilkinson type models of interface dynamics, *Phys. Rev. E* **54**, 2256 (1996).
- [73] B. Wang, S. M. Anthony, S. C. Bae, and S. Granick, Anomalous yet brownian, *Proceedings of the National Academy of Sciences* **106**, 15160 (2009).
- [74] B. Wang, J. Kuo, S. C. Bae, and S. Granick, When brownian diffusion is not gaussian, *Nature materials* **11**, 481 (2012).
- [75] A. V. Chechkin, F. Seno, R. Metzler, and I. M. Sokolov, Brownian yet non-gaussian diffusion: from superstatistics to subordination of diffusing diffusivities, *Physical Review X* **7**, 021002 (2017).